RSC Sustainability

ROYAL SOCIETY OF CHEMISTRY

PAPER

View Article Online
View Journal | View Issue

Check for updates

Cite this: *RSC Sustainability*, 2025, **3**, 510

Photodegradation of berberine hydrochloride at the interface of 1D–2D nanohybrid of nickel ferrite supported on reduced graphene oxide†

Sayanika Saikia,[a] Salma A. Khanam,[a] Priyanuj Kandali,[a] Ankur Kanti Guha [b] and Kusum K. Bania *[a]

Morphologically tuned one-dimensional (1D) nickel ferrite ($NiFe_2O_4$) nanorod (NFNR) was synthesized through co-precipitation and hydrothermal methods. The NFNR was combined with two-dimensional (2D) reduced graphene oxide (rGO) derived from battery waste and designated as NFNR/rGO. The 1D–2D nanohybrid was used as a UV-light-harvesting photocatalyst for the degradation of berberine hydrochloride (BH), a hazardous water contaminant. Using NFNR/rGO, 97.61% of BH was degraded in 60 min upon exposure to UV light along with 83.87% of mineralization following the first-order kinetics. The present analysis showed that NFNR/rGO exhibited 4.8 times higher photocatalytic activity than the bare NFNR owing to increased surface area, reduced indirect band gap, more active sites and low charge recombination rate. The photocatalytic degradation mechanism of BH was investigated and examined with the help of trapping experiments and photoluminescence (PL) spectroscopy. The experimental evidences demonstrated that $OH^{\bullet}$ (hydroxyl) and $O_2^{-\bullet}$ (superoxide) radicals played dominant roles in the photodegradation procedure. The various probable intermediates involved during the reaction were investigated through liquid chromatography-mass spectrometry (LCMS). The magnetically separable catalyst was reused and assessed for five consecutive cycles. The photocatalyst delivered strong activity towards the photodegradation of BH during recycling. The photodegradation process of BH was also studied using three other catalysts having variable molar ratios of Ni to Fe, and it was found that NFNR/rGO with Ni : Fe = 1 : 2 exhibited a superior activity.

Received 11th October 2024
Accepted 30th November 2024

DOI: 10.1039/d4su00638k

rsc.li/rscsus

Sustainability spotlight

In today's world, which is suffering from environmental pollution, climate change and global warming, "sustainability" is under threat, and realizing a sustainable world is challenging unless necessary steps are taken to have control over causes that are hampering the global environment. One such cause is the berberine hydrochloride (BH) antibiotic, a pharmaceutical waste considered to be toxic to water bodies. According to published research, every ton of antibiotics generated will yield 500–6500 m^3 of wastewater, which includes significantly more organic pollutants than domestic sewage. BH is a frequently released antibiotic to the aquatic system and has significant potential hazards and negative effects on the ecosystem and human health. However, photocatalysis is an energy-efficient, green process that utilizes light to drive chemical reactions, contributing to sustainability by enabling pollution reduction and production of renewable energy. In this work, we designed a 1D–2D nanohybrid photocatalyst of nickel ferrite ($NiFe_2O_4$) and reduced graphene oxide (rGO) that can effectively degrade BH within 60 min under UV light irradiation. The 1D $NiFe_2O_4$ nanorod composite with 2D rGO nanosheets can remove BH effectively up to 250 ppm with ~84% of mineralization. Hence, we believe that the designed catalyst can be explored for practical applications to degrade BH as its toxicity has become a major concern.

[a]*Department of Chemical Sciences, Tezpur University, Assam, 784028, India. E-mail: kusum@tezu.ernet.in; bania.kusum8@gmail.com*

[b]*Advanced Computational Chemistry Centre, Cotton University, Panbazar, Guwahati, Assam 781001, India*

† Electronic supplementary information (ESI) available: Physical measurements; synthesis procedure of Fe_2O_3 and NiO; FTIR spectra of NFNR, rGO and NFNR/rGO; TGA spectra of NFNR, rGO and NFNR/rGO; N_2 adsorption–desorption isotherm of NFNR/rGO; Nyquist plot of NFNR, NFNR/rGO and rGO; UV spectra and bar diagram of BH degradation for different prepared catalysts (2 mg) with 90 min UV light irradiation; UV spectra and bar diagram for the comparison of BH degradation under the conditions of darkness, room light and UV light irradiation with NFNR/rGO (2 mg) and 90 min irradiation; point of zero charge (pH_{PZC}) of NFNR/rGO; UV spectra and bar diagram showing the effect of pH on BH degradation; UV spectra and bar diagram of BH degradation for different initial concentrations of the BH solution; linear relationship of absorbance *vs.* concentration of BH; kinetics analysis of BH degradation with the NFNR, rGO, and NFNR/rGO composite; comparison of the BH degradation efficiency of the NFNR/rGO composite with a physical mixture of NFNRs and rGO; percentage mineralization efficiency of BH using NFNR/rGO; stability test of NFNR/rGO under strong acidic conditions (pH = 2); effect of various scavenging agents ($AgNO_3$, KI, isopropanol and ascorbic acid) on BH degradation; ESR analysis; PXRD, Raman, FTIR spectra, TGA and SEM-EDX pattern of the other synthesized catalysts: NFNR-1/rGO, NFNR-2/rGO, NFNR/CTW, Fe_2O_3 and NiO; photocatalytic degradation of BH with other synthesized catalysts under optimized conditions; comparative study of the efficiency of nickel ferrite photocatalysts for organic pollutant degradation. See DOI: https://doi.org/10.1039/d4su00638k

Open Access Article. Published on 16 December 2024. Downloaded on 2/8/2026 9:00:53 AM. This article is licensed under a Creative Commons Attribution-NonCommercial 3.0 Unported Licence.

© 2025 The Author(s). Published by the Royal Society of Chemistry

Open Access Article. Published on 16 December 2024. Downloaded on 2/8/2026 9:00:53 AM.
This article is licensed under a Creative Commons Attribution-NonCommercial 3.0 Unported Licence.

1. Introduction

Light-harvesting semiconducting materials have become promising photocatalysts for energy production as well as to remove water pollutants.[1] However, the property of such materials depends on various factors like size, shape and dimension. They may have dimensions ranging from zero to three, each having unique properties. The one-dimensional (1D) nanomaterials can be synthesized as nanorods, nanotubes or as wires and belts.[2] Due to good surface area and formation of a desirable number of active sites on their surface, the 1D nanomaterials can facilitate different photocatalytic reactions.[3] The main advantages of these types of nanomaterials are that they form sites for the adsorption of reactant molecules.[4] At the same time, the surface active sites can significantly perform charge separation and thereby accelerate the reactions at the interface.[5] The 1D material with nanorod or nanotube structures can further be beneficial in photocatalytic reactions as their photo adsorption, light scattering, and charge transport ability (electrons and holes) can be modulated by tuning their length and diameter.[6] Due to such benefits and high prospects of 1D nanomaterials in the field of energy and environment, a good number of research work have been devoted towards large-scale synthesis of 1D photocatalysts.[7,8]

The 1D photocatalysts pave a new path in the field of clean energy, environment and sustainability.[9] However, the fast recombination rate of electrons and holes makes them less productive and selective in photocatalytic reactions.[6] Therefore, to overcome these problems, the 1D materials are combined with other materials such as 2D nanomaterials to lower the charge recombination rate.[10] The 1D nanostructure of metal oxides such as TiO_2, ZnO, Fe_3O_4, V_2O_5, and WO_3 is well explored for different photocatalytic and photodegradation processes.[10–14] The activities of these metal oxides are found to be significantly altered through the construction of their heterojunctions or by creating some defect sites or by doping of metals having surface plasmon effects.[15,16] In this regard, nickel ferrites ($NiFe_2O_4$) are one such mixed metal oxides that have been extensively studied as photocatalysts for different applications such as photocatalytic water splitting reaction and water purification.[17,18] The spinel $NiFe_2O_4$ of different dimensions and morphologies is recognized to have better magnetic, electrical and thermochemical properties, and investigated as magnetically separable nanophotocatalysts.[19]

The photocatalytic activity of $NiFe_2O_4$ has been improvised *via* various modifications such as heterojunction formation, doping with other elements, and composite material formation.[20,21] For example, He *et al.* synthesized a nanocomposite of $NiFe_2O_4$ and $Bi_{24}O_{31}Br_{10}$ by a hydrothermal method for the degradation of crystal violet dye under visible light illumination,[22] Xia *et al.* combined $SrTiO_3$ spheroidal nanoparticles with $NiFe_2O_4$ polyhedra for the photodegradation of RhB.[23] Dharmaraja *et al.* demonstrated the effectiveness of porous ZnS/$NiFe_2O_4$ nanocomposites towards the breakdown of dyes under solar radiation.[18] Taj and his co-workers demonstrated the efficacy of $NiFe_2O_4$ towards the removal of two water pollutants, namely, ciprofloxacin and Congo red.[24] Recently, an N-doped nickel ferrite was created by Patar *et al.* to aid in the photodegradation of LEV and CIP antibiotics.[25] Additionally, supports such as graphene oxide or such conducting materials facilitate the photocatalytic degradation process by providing good surface area, improving electron mobility and surface adsorption sites, and enhancing the stability.[26]

Berberine hydrochloride (BH) is one of the frequently used isoquinoline alkaloids well known for wide-spectrum antibiotics in human medicine. The contamination of BH in the aquatic environment affects the water quality, making it unfit for direct human consumption.[27] Moreover, BH is reported to have the ability to disrupt the life cycle of microorganisms and prevent them from reproduction.[28] As the biological treatment of the BH wastewater is not acceptable, there is a demand for the development of an energy-efficient and environmentally friendly process with a high BH elimination potency. A number of techniques including ozonation,[29] physical adsorption,[30] microwave reduction,[31] flocculation,[32] Fenton process,[33] photo-Fenton process,[34] and piezocatalysis[35–37] are known for the removal of different organic pollutants. However, each of these processes has certain limitations, and some processes require external chemicals and energy. Therefore, currently, the photodegradation of dye contaminants, antibiotics and such organic pollutants in water bodies using light-harvesting semiconducting materials and nanocomposites appears to be an energy-efficient, environmentally benign and greener technique.[38–40] Nevertheless, using conventional water treatment methods to totally decompose BH is still a challenge. In this regard, the photodegradation of these organic contaminants using semiconductors is recognized to be one of the green protocols. For example, Yu *et al.* constructed a $TiO_2/SiO_2/g\text{-}C_3N_4$ heterostructure for the adsorption and photocatalytic degradation of berberine under visible light.[27] Rabé *et al.* used cathodic WO_3 and anodic $g\text{-}C_3N_4/Fe^0/TiO_2$ for the breakdown of berberine chloride under visible light.[41]

Although a good number of studies have been conducted on similar systems, to the best of our knowledge, the 1D nanostructure of $NiFe_2O_4$ has not yet been reported for the photodegradation of antibiotic pharmaceutical pollutants such as berberine hydrochloride (BH). Therefore, considering the ability of $NiFe_2O_4$ as a photocatalyst and the toxicity and adverse impact of BH on water bodies, in this work, we constructed a heterojunction by combining a 1D $NiFe_2O_4$ nanostructure with 2D reduced graphene oxide nanosheets derived from battery and tea wastes. The current study not only focuses on lowering the electron–hole recombination rate at the $NiFe_2O_4$ nanorod surface but also emphasizes on waste management, whereby waste batteries and tea waste leaves are converted into useful charge carriers and promoters.

2. Experimental section

2.1. Chemicals

Iron chloride anhydrous ($FeCl_3$, pure ≥98%), nickel sulphate heptahydrate ($NiSO_4 \cdot 7H_2O$, pure, 98%), hydrochloric acid (HCl), sulfuric acid (H_2SO_4) (95.0–98%) and nitric acid (HNO_3) were purchased from E-Merck. Berberine hydrochloride (pure, >98%), potassium nitrate (KNO_3, pure, >99%), sodium lauryl sulfate

Open Access Article. Published on 16 December 2024. Downloaded on 2/8/2026 9:00:53 AM. This article is licensed under a Creative Commons Attribution-NonCommercial 3.0 Unported Licence.

$(CH_3(CH_2)_{11}OSO_3Na$, ≥97%) and Mohr's salt $[Fe(NH_4)_2(SO_4)_2 \cdot 6H_2O]$ were provided by TCI. From E-Merck, the terephthalic acid (98%), sodium hydroxide (NaOH, pure, >99%), ascorbic acid (99.0–100.5%), ethanol (>99% pure), tartaric acid (99.7–100.5%), potassium iodide (KI, pure 99%), silver nitrate ($AgNO_3$, 99%), potassium ferricyanide (99%), dimethylglyoxime (DMG, ≥99%), and 5,5-dimethyl-1-pyrroline N-oxide (DMPO, ≥97%) were obtained.

2.2. Synthesis of nickel ferrite nanorods (NFNRs)

The nickel ferrite nanorods designated as NFNRs were prepared by stirring a mixture of 1 mol $NiSO_4 \cdot 7H_2O$ and 2 mol $FeCl_3$ dissolved in 100 mL of distilled water (Scheme 1a). A specified quantity of sodium lauryl sulfate (SLS) (1 mmol, 288.38 mg in a little amount of water) was added as the surfactant, followed by further stirring. After that, the aforementioned salt solution was agitated for one hour at around 80 °C and then 1 M NaOH solution was slowly added dropwise till its pH raised to about 13. Through centrifugation, brown coloured precipitates were obtained and washed thoroughly to eliminate extra surfactants and undesired contaminants, and the solid residue was oven-dried for 1 h at around 90 °C. At last, the product was subjected for calcination at 700 °C for 3 h to get the nanorod structure of nickel ferrite.

2.3. Synthesis of carbon materials from battery and tea wastes

For the modification of the above-synthesized NFNRs, in this work we used two different carbon materials: one derived from battery wastes and the other derived from waste tea leaves, as described in our previous work.[42,43] Both these materials were obtained by the modified Hummer's approach. The battery waste-derived carbon material was recognized to be reduced graphene oxide (rGO) and that obtained from tea waste was designated as Carbon Tea Waste (CTW).

2.4. Synthesis of photocatalysts

In order to synthesize NFNR/rGO composites, a stable suspension of rGO was prepared by dispersing 0.1 g of dry rGO in distilled water (100 mL) and then ultrasonicated for 30 min. After that rGO suspension was mixed with NFNR and subsequently subjected to hydrothermal treatment at 80 °C for 2 h (Scheme 1b). The residue obtained after filtration was washed with distilled water, and then vacuum dried at 80 °C for 1 h.

Following a similar procedure, three other materials, namely, NFNR-1/rGO, NFNR-2/rGO, and NFNR/CTW were synthesized by varying the metal concentration and the carbon matrix. The molar ratios of Ni and Fe salts in NFNR-1/rGO and NFNR-2/rGO were maintained at 1 : 1 and 2 : 1, respectively during the synthesis. The NFNR/CTW material was prepared by using Ni and Fe salts in 1 : 2 molar ratio and replacing rGO with CTW. For a comparative study, nickel oxide (NiO) and iron oxide (Fe_2O_3) were prepared by following the reported procedures (provided in the ESI†).[44,45]

2.5. Procedure for the photodegradation of berberine hydrochloride (BH) antibiotics

The degradation of BH under UV-visible light (450 W Hg lamp, λ = 254 nm) was measured using 12 mg of the synthesized photocatalyst in 20 mL of 50 ppm aqueous BH solution at pH = 2. The detail of the photoreactor is provided in our previous work.[43] The mixture was kept in the darkness for 30 min to achieve equilibrium between the NFNR/rGO (photocatalyst) and BH. A certain volume of the reaction mixture was collected at a certain time interval throughout the photocatalytic reaction. The UV-visible spectroscopy was employed to assess the concentration of BH in the solution, measuring absorbance at a distinctive wavelength of 354 nm. The photocatalytic efficiency of the catalyst was measured by calculating the C_t/C_o value using eqn (1):[41]

$$\%\text{Reduction/degradation} = 1 - \frac{C_t}{C_o} \times 100 \quad (1)$$

where C_o = initial concentration, C_t = concentration at different time periods.

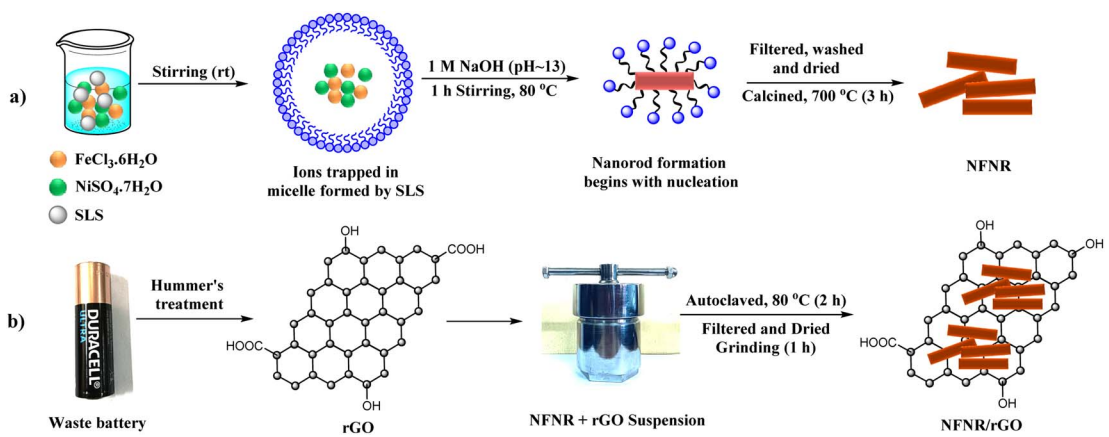

Scheme 1 Synthesis of (a) NFNR and (b) NFNR/rGO composites.

© 2025 The Author(s). Published by the Royal Society of Chemistry

Open Access Article. Published on 16 December 2024. Downloaded on 2/8/2026 9:00:53 AM.
This article is licensed under a Creative Commons Attribution-NonCommercial 3.0 Unported Licence.

The organic matter present in the antibiotic sample was calculated using the Walkley and Black titration method as reported before using the following formula:[46]

$$\text{Total organic carbon, TOC}(\%) = \frac{0.003\ \text{g} \times A \times (B - C) \times 100}{W(\text{g})} \quad (2)$$

A = molarity of Fe $(NH_4)_2(SO_4)_2$ solution, B = blank titration value, C = titration value of sample, W = sample weight in gram.

2.6. Computational details

A model cluster considering three nickel (Ni) centres, three iron (Fe) centres and two oxygen (O) centres embedded on a small unit of rGO was constructed for the theoretical study. The model was fully optimized at the M06-2X/def2-TZVP level[47] and found to be a true minimum on the potential energy surface. All these calculations were performed using the Gaussian 16 suite of program.[48] The charge density difference and projected density of states (PDOS) were calculated using the Multiwfn program code.[49]

3. Results and discussions

The PXRD patterns of spinel nickel ferrite ($NiFe_2O_4$) nanorods (NFNRs) and the composite of NFNRs loaded with rGO (NFNR/rGO) are compared in Fig. 1a. In the PXRD pattern of rGO (Fig. 1a, black line), a broad peak at a 2θ value of 24.20° was observed due to the (002) plane.[43] A less prominent peak at 2θ = 42.9° with a (001) orientation appeared for the imperfect graphite crystal.[50] Additionally, a diffraction peak at 26.4° indicated the presence of small impurities of graphite. In the synthesized NFNR material, the diffraction peak at 30.3°, 35.5°, 37.1°, 43.3°, 53.9°, 57.4°, 62.9°and 74.8° matched well with the crystalline planes of $NiFe_2O_4$ at (220), (311), (222), (400), (422), (511), (440) and (566), respectively, as shown in Fig. 1a (red line, JCPDS No. 00-003-0875). The NFNR sample showed a very less intensity peak at 33.05°, implying small amounts of impurities of Fe_2O_3 in the synthesized material (JCPDS no. 00-024-0072). The PXRD pattern of the NFNR/rGO compound showed the diffraction peaks of both NFNR and rGO, indicating the formation of the desired material.

The Raman lines of the NFNR, rGO and NFNR/rGO composite are depicted in Fig. 1b. The rGO (black line) material showed two significant peaks of graphitic materials: D band at 1353 cm^{-1} and G band at 1598 cm^{-1}.[43] NFNR showed a band at 704 cm^{-1} consistent with the A_{1g} symmetry (Fig. 1b, red line).[51] The peak at 323 cm^{-1} correlated with the E_g mode and other three T_{2g} modes were obtained at 195 cm^{-1}, 484 cm^{-1} and 574 cm^{-1}.[52] The presence of all the rGO and NFNR characteristic peaks in the composite material (Fig. 1b, blue line) demonstrated the well mixing of NFNR and rGO forming the NFNR/rGO composite.

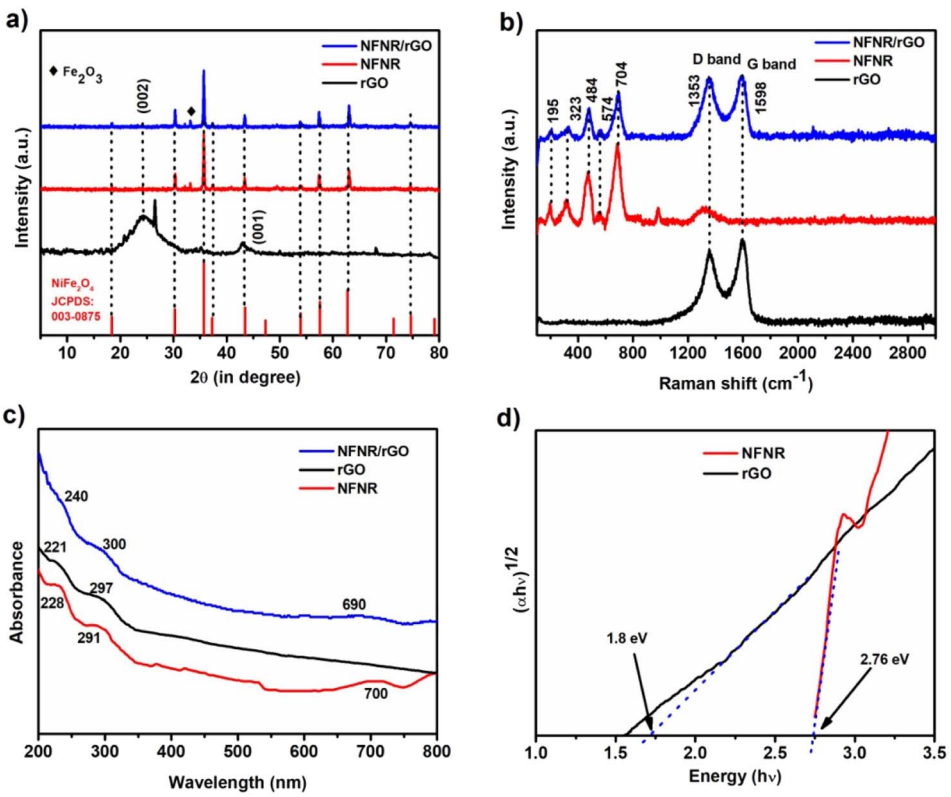

Fig. 1 (a) PXRD patterns, (b) Raman spectra, (c) UV visible spectra of rGO (black), NFNR (red) and NFNR/rGO (blue), and (d) Tauc plot of NFNR (red) and rGO (black).

Open Access Article. Published on 16 December 2024. Downloaded on 2/8/2026 9:00:53 AM.
This article is licensed under a Creative Commons Attribution-NonCommercial 3.0 Unported Licence.

The UV-visible DRS (Diffuse Reflectance Spectra) of NFNR/rGO, NFNR and rGO are displayed in Fig. 1c. The peaks at 221 nm and 297 nm were characteristic peaks of rGO (black line), assigned to the π–π* transition of C=C bonds and n–π* transition of C=O bonds respectively.[53] Two broad absorption peaks were present at 228 nm and 291 nm in the NFNR. In comparison to pure NFNR, a noticeable red shift at the absorption edge in NFNR/rGO indicated that the incorporation of rGO has reduced the band gap of the NFNR.[54] The broad peaks at 690 nm in the NFNR and at 700 nm in NFNR/rGO were assigned to d–d transition in metal oxides. The band gap energy was calculated using the Kubelka–Munk equation:[55]

$$(\alpha h\nu)^n = k(h\nu - E_g) \quad (3)$$

where k = proportionality constant, E_g = optical band gap energy, ν = frequency of light, n = nature of electronic transition, α = absorption coefficient.

The indirect band gap (E_g) was calculated from the extended linear portion of the curve plotted between $(\alpha h\nu)^{1/2}$ and $h\nu$ to the energy axis considering $n = 1/2$. The E_g value of the NFNR and rGO was determined to be 2.76 eV and 1.8 eV, respectively (Fig. 1d). The band gap values were found to be close to those reported ones.[25,56] Therefore, based on the measured E_g value, the synthesized materials were used as photocatalysts.

Additionally, we performed a theoretical analysis to predict the charge densities and the density of states (DOS), considering a small model system of nickel ferrites (three nickel (Ni) centres, three iron (Fe) centres and two oxygen (O) centres). We performed the Density Functional Theory (DFT) calculation and optimized the local minimum geometry of the model complex, as shown in Fig. 2a. The nickel ferrite system was held tightly by the oxygen atom of the –OH functional group of rGO (Fig. 2a). From the charge density calculation, it was found that the charges lost at the Ni centre got accumulated in the Fe centre (Fig. 2b). The density of state calculation was performed for rGO, nickel ferrite system and nickel ferrite system embedded on rGO. The Fermi level of the bare rGO lay at −3.5 eV (Fig. 2c), while the bare Nickel ferrite system lay at −3.7 eV (Fig. 2d),

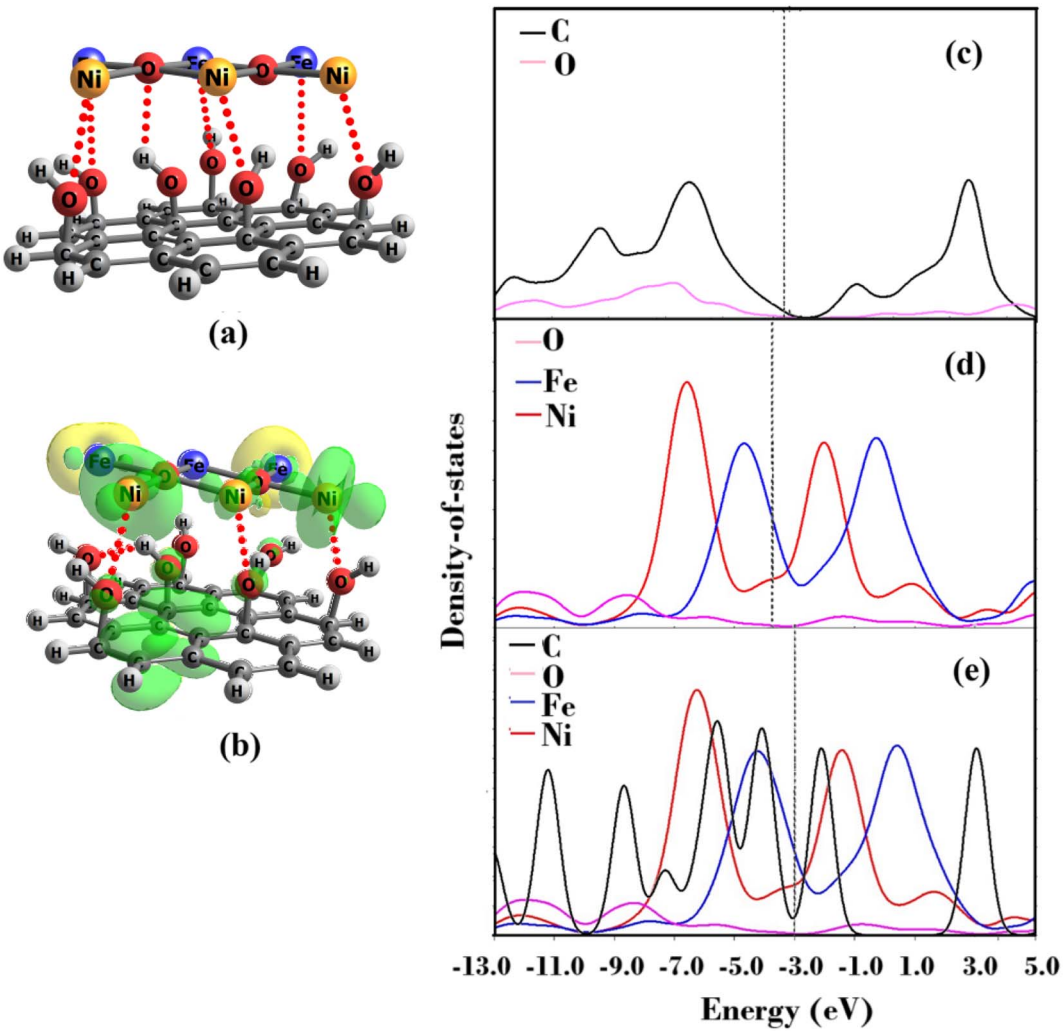

Fig. 2 (a) Optimized local minimum geometry of the model complex, (b) charge density difference plot of the model complex (yellow = charge increment, green = charge depletion) and (c) projected density of states (PDOS) of bare rGO, (d) bare Nickel ferrite system and (e) PDOS of the Nickel ferrite system embedded in rGO. The dotted line represents the Fermi level.

© 2025 The Author(s). Published by the Royal Society of Chemistry

Open Access Article. Published on 16 December 2024. Downloaded on 2/8/2026 9:00:53 AM.
This article is licensed under a Creative Commons Attribution-NonCommercial 3.0 Unported Licence.

which shifted towards right (−3.0 eV) in the Nickel ferrite system embedded in rGO (Fig. 2e). This implied that the presence of rGO can shift the Fermi level of the Nickel ferrite system, thereby influencing the photocatalytic activity.

The Fourier Transform Infrared Spectroscopy (FTIR) spectra of the synthesized materials are depicted in Fig. S1:† rGO (black), NFNR (red) and NFNR/rGO (blue). In rGO, the peaks at 2926 cm^{-1} and 2849 cm^{-1} are responsible for the asymmetric $\nu_{as}(-CH_2)$ and symmetric $\nu_s(-CH_2)$ stretching vibrations of rGO (Fig. S1† (black line)).[42] The smaller intensity peaks at 1642 cm^{-1} and 1585 cm^{-1} were assigned to the C–OH, COOH and C–O groups on the rGO matrix.[57] The FTIR spectrum of the synthesized NFNR sample displayed two bands at 595 cm^{-1} associated with Ni–O stretching with tetrahedral coordination and at 420 cm^{-1} assigned to the vibration of the octahedrally coordinated Fe–O bond. Furthermore, the band at 1112 cm^{-1} and 3443 cm^{-1} was linked to the vibration modes of the C–O group and the symmetric vibration of the –OH group, respectively, Fig. S1† (red line).[58] These vibrational bands were well retained in the composite material, confirming the combination of the rGO matrix with NFNR (Fig. S1,† blue line).

Thermogravimetric analysis (TGA) was implemented to know the thermal stability of the prepared samples (Fig. S2†). The TGA spectra of NFNR (Fig. S2a,† red line) showed an initial sharp weight loss of 3% followed by a slow decomposition of 2.5% up to 350 °C due to moisture evaporation.[59] After that, a major weight loss occurs at 400–600 °C. After combination with rGO, the material obtained high stability as the TGA profile represented only a slight loss in the weight percentage (Fig.-S2a,† blue line). The enhancement in such thermal stability was attributed to the impact of rGO as rGO itself has good thermal stability, as predicted from the TGA profile as shown in Fig. S2b.† The N_2 adsorption–desorption isotherm of NFNR/rGO is shown in Fig. S3.† From the Brunauer–Emmett–Teller (BET) analysis, the surface area of NFNR/rGO was found to be 120.01 $m^2\ g^{-1}$.

The morphology and the structural integrity of the materials were analyzed by electron microscopy imaging techniques, namely, Scanning Electron Microscopy (SEM) and Transmission Electron Microscopy (TEM). The elemental compositions were determined by Energy-Dispersive X-ray Spectroscopy (EDX) analysis. The SEM images revealed the formation of nanorod structures of $NiFe_2O_4$ (Fig. 3a–d), and also their proper combination with the rGO matrix, as shown in Fig. 3e and f. The nanorods were clearly visible in the TEM images along with their connection with the rGO matrix (Fig. 4a–d). Fig. 4c and d show the distinct structure of NFNR nanorods that were evenly distributed on the rGO surface. The nanorods were formed within a length of 70–90 nm and a diameter of 10–20 nm (Fig. 4b). The fringes of the NFNR/rGO nanocomposite are shown in Fig. 4e and f. The lattice spacing determined from these HRTEM (High Resolution Transmission Electron Microscopy) images were 0.29, 0.461, and 0.262 nm, corresponding to the (220), (111), and (311) planes of $NiFe_2O_4$. Furthermore, a lattice spacing of 0.25 nm (Fig. 4f) was in agreement with the (311) plane of $NiFe_2O_4$. The existence of all the characteristic elements Fe, Ni, O was ascertained from the EDX-spectra. The Cu appeared from the Cu-grid used during the analysis. Fig. 4g and h demonstrate the weight percentages of the elements present in the material. It was found that Fe has higher atomic % than Ni in the catalyst surface. From Inductively Coupled Plasma Optical Emission Spectrophotometer (ICP-OES) analysis, the ratio of Ni (149.1 μg L^{-1}) and Fe (344.2 μg L^{-1}) in NFNR/rGO was found to be ~1 : 2.

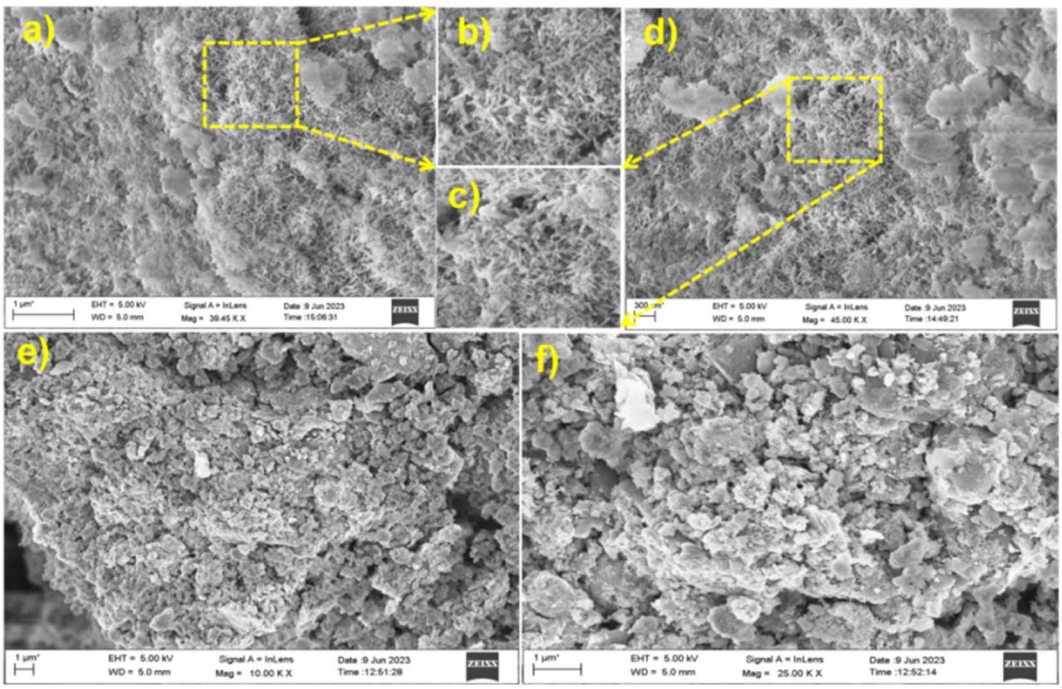

Fig. 3 (a and d) SEM images of NFNR; (b and c) zoom image of (a and d), and (e and f) SEM images of NFNR/rGO.

Open Access Article. Published on 16 December 2024. Downloaded on 2/8/2026 9:00:53 AM.
This article is licensed under a Creative Commons Attribution-NonCommercial 3.0 Unported Licence.

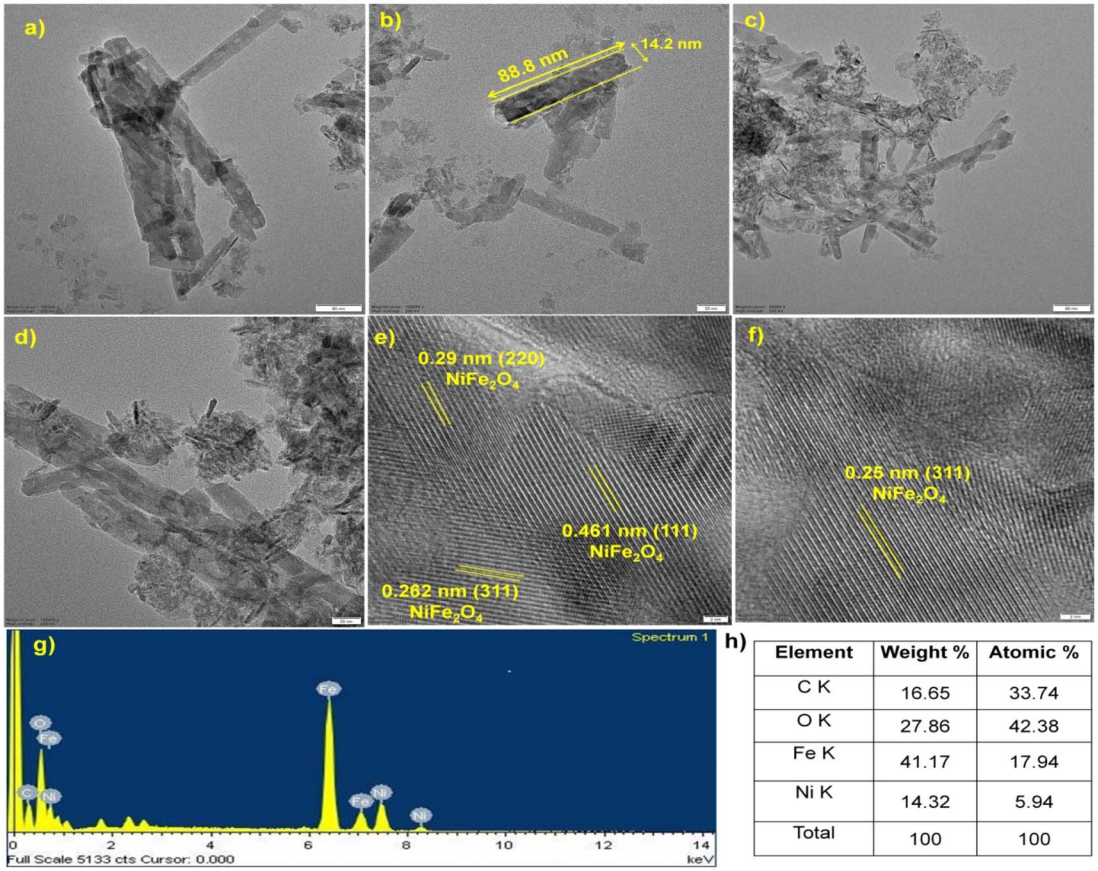

Element	Weight %	Atomic %
C K	16.65	33.74
O K	27.86	42.38
Fe K	41.17	17.94
Ni K	14.32	5.94
Total	100	100

Fig. 4 TEM image of (a and b) NFNR, (c and d) NFNR/rGO showing the nanorod structure distributed on the rGO surface, (e and f) fringe pattern of NFNR/rGO obtained from HRTEM analysis, (g) EDX spectra and (h) average elemental distribution in the NFNR/rGO material.

The Mott–Schottky (MS) plots were analyzed to ascertain the flat band potentials (V_{fb}) and type of semiconductors, based on the impedance measurement, as shown in Fig. 5a. Both the NFNR and rGO showed a positive slope, indicating the *n*-type semiconductor characteristics of the materials.[60] Additionally, after projecting the graph to $C^{-2} = 0$, the V_{fb} values for the NFNR and rGO were calculated from the *x*-axis intercept. The calculated V_{fb} values for the NFNR and rGO were −1.16 V and −0.55 V *vs.* RHE (Fig. 5a). Usually, the V_{fb} values are observed to be 0.1 V above the conduction band potential (V_{CB}) for *n*-type semiconductor materials.[61] Therefore, the V_{CB} values of the NFNR and rGO materials were estimated to be −1.26 V and −0.65 V (*vs.* RHE), respectively. Using band gap values from DRS analysis and V_{CB}, the valence band potentials (V_{VB}) of NFNR and rGO were calculated to be 1.5 V and 1.15 V *vs.* RHE, respectively (Fig. 5b).

The charge movement, exchange, and recombination rate of the photo-induced electron–hole pairs in the composite can be explained by examining the photoluminescence (PL) patterns. A lower PL intensity is often associated with a lower electron–hole recombination rate leading to a greater photocatalytic activity. The PL spectra of NFNR, rGO and NFNR/rGO at an excitation wavelength of 425 nm are displayed in Fig. 5c.[62] All the materials showed an emission peak at 582 nm. The intensity of PL signal for NFNR/rGO was lower; suggesting that the rate of electron–hole recombination for NFNR/rGO was effectively inhibited. To check the electron–hole separation capacity, the photocurrent measurement was performed (Fig. 5d). The analysis indicated that NFNR/rGO showed the highest photocurrent response compared to the bare NFNR and rGO, indicating a higher degree of charge separation. Fig. S4† displays the Nyquist plots of the electrochemical impedance spectroscopy (EIS) data for the NFNR (red line), rGO (black line) and NFNR/rGO nanocomposite (blue line). According to the Nyquist plot, charge-separation rate of the working electrode improves with a lower arc radius.[63] The NFNR/rGO sample had a smaller circular radius than that of the pure NFNR and rGO, indicating lower resistance and higher charge separation. Therefore, EIS results indicated that the NFNR/rGO nanocomposite was superior to the NFNR in terms of charge transfer efficiency.

X-ray photoelectron spectroscopy (XPS) spectra of the NFNR and NFNR/rGO composite material were examined to determine the elemental oxidation states. Based on the XPS spectra displayed in Fig. 6a and b, Fe and Ni were found in the +3 and +2 oxidation states, respectively. The detailed description of all the binding energy (B. E.) values is given in Table 1. In the case of the O 1s spectra, the peak at 533.4 eV represented the M–O–M bond, whereas the remaining two peaks were associated with the functional groups of rGO (Fig. 6c). The XPS spectra of C 1s showed three distinct peaks in NFNR/rGO, characteristic of C=

© 2025 The Author(s). Published by the Royal Society of Chemistry

Open Access Article. Published on 16 December 2024. Downloaded on 2/8/2026 9:00:53 AM.
This article is licensed under a Creative Commons Attribution-NonCommercial 3.0 Unported Licence.

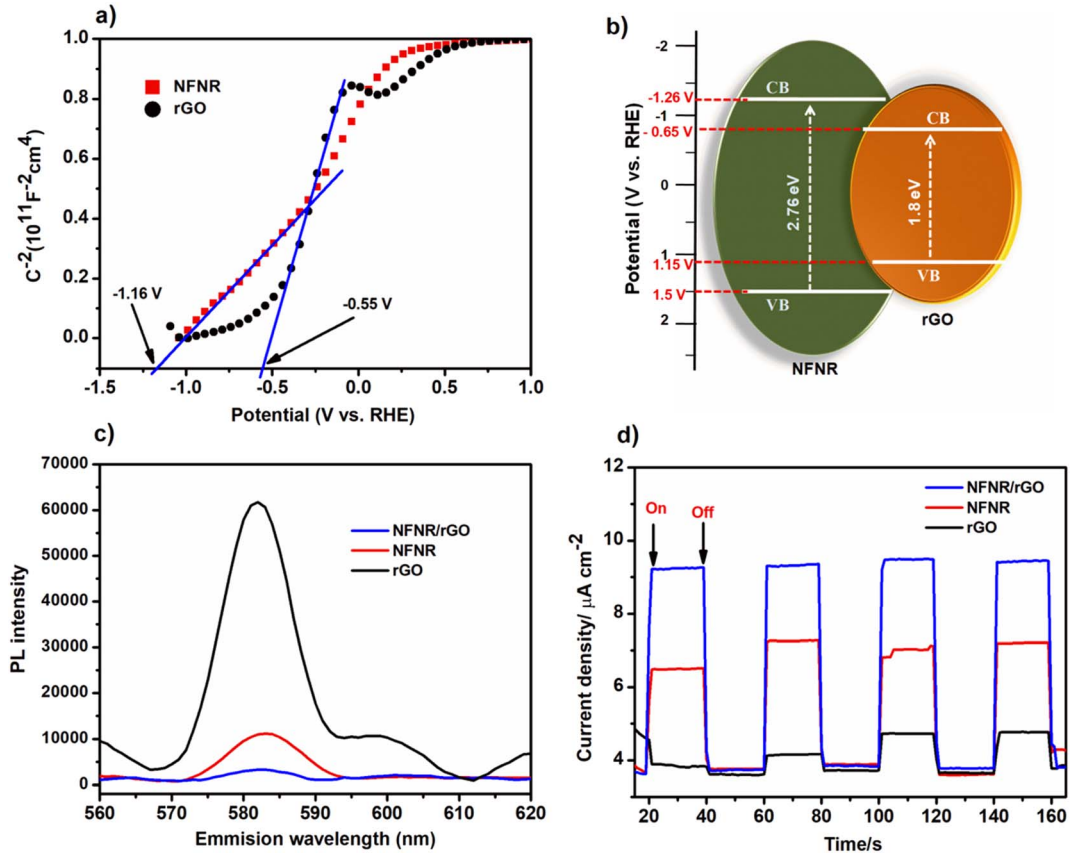

Fig. 5 (a) Mott–Schottky plot for the flat band potential (V_{fb}) of the NFNR (red line) and rGO (back line), (b) band edge structure showing the CB and VB potential of the NFNR and rGO, (c) PL spectra and (d) photocurrent responses of rGO (black line), NFNR (red line) and NFNR/rGO (blue line).

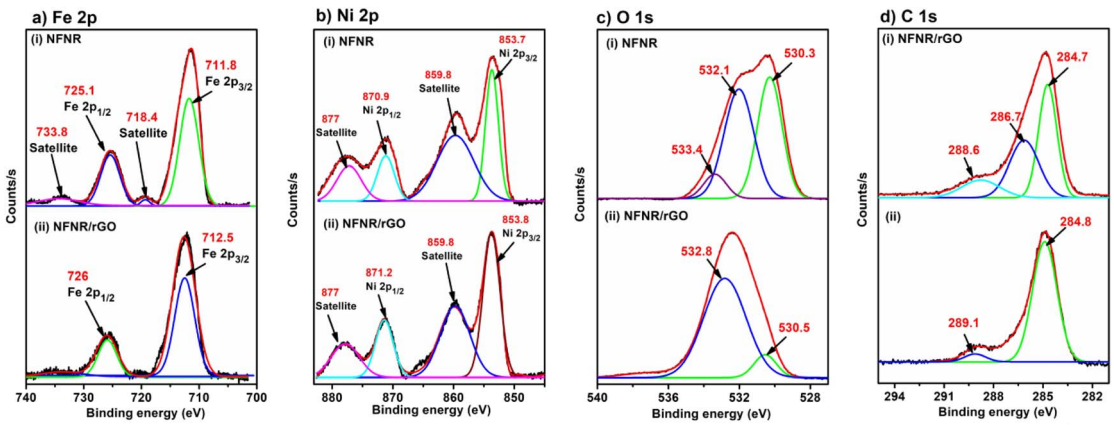

Fig. 6 XPS spectra of (a) Fe 2p, (b) Ni 2p, and (c) O 1s present in (i) NFNR and (ii) NFNR/rGO, and (d) (i) C 1s present in NFNR/rGO and (ii) C 1s XPS spectra taken as reference.

C/C–C (284.7 eV), C–O (286.7 eV) and O–C–O/O–C=O (288.6 eV) (Fig. 6d(i)). All the XPS peaks are fitted with respect to C 1s, as shown in Fig. 6d(ii).

4. Photocatalytic activity study

The photocatalytic activity of the synthesized materials was evaluated for the degradation of BH under UV light exposure. For the photodegradation process, 20 mL of a 50 ppm aqueous BH solution was taken. Considering 2 mg of each NFNR and

Open Access Article. Published on 16 December 2024. Downloaded on 2/8/2026 9:00:53 AM. This article is licensed under a Creative Commons Attribution-NonCommercial 3.0 Unported Licence.

Table 1 Comparative XPS analysis data of NFNR/rGO with the NFNR

Element		Peak	NFNR (eV)	Δ_{metal} ($2p_{1/2}$–$2p_{3/2}$)	NFNR/rGO (eV)	Δ_{metal} ($2p_{1/2}$–$2p_{3/2}$)	Assignment	Ref.
Fe	Fe 2p	Fe $2p_{3/2}$	711.8	13.3 eV	712.5	13.5 eV	Fe(III)	64
		Fe $2p_{1/2}$	725.1		726		Fe(III)	
		Satellite	718.4, 733.8					
Ni	Ni 2p	Ni $2p_{3/2}$	853.7	17.2 eV	853.8	17.4 eV	Ni(II)	65 and 66
		Ni $2p_{1/2}$	870.9		871.2		Ni(II)	
		Satellite	859.8, 877		859.8, 877			
O	O 1s		530.3		530.5		Functional groups of rGO	64
			532.1		532.8			
			533.4				M–O–M	
C	C 1s				284.7		(C=C/C–C)	64
					286.7		(C–O)	
					288.6		(O–C–O/O–C=O)	

NFNR/rGO catalyst at pH = 2, the photo-irradiation was done for 90 min in individual cases. Under this condition, the NFNR showed 15.15% degradation of BH, while NFNR/rGO led to 40% degradation (Fig. S5a and b†). As mentioned in the introduction, the 1D nanostructure has a faster charge recombination rate. Therefore, probably in the NFNR, without the rGO matrix, the electron–hole separation tendency is less and thereby leads to poor photodegradation ability. Therefore, further studies were conducted with the NFNR/rGO photocatalyst.

Initially, a blank experiment was conducted in the presence of light without any photocatalyst. However, after 2 h of UV light exposure, no decolorization of the BH sample or alteration of UV spectra was seen. Additional investigations were carried out at room light and dark conditions in the presence of 2 mg of NFNR/rGO (pH = 2), and the results are shown in Fig. S6a.† Under this condition, only 9.85% and 18.8% degradation of BH occurred in the darkness and room light, respectively (Fig. S6b†). It was thus established from the aforementioned findings that UV light and the photocatalyst were both crucial for the degrading process of BH. Keeping all other conditions to be the same (20 mL 50 ppm BH solution, 2 mg catalyst and pH = 2), the impact of irradiation time was monitored. For this, the photocatalytic degradation of BH was studied in a time window of 15–90 min, and the optimized irradiation time was estimated

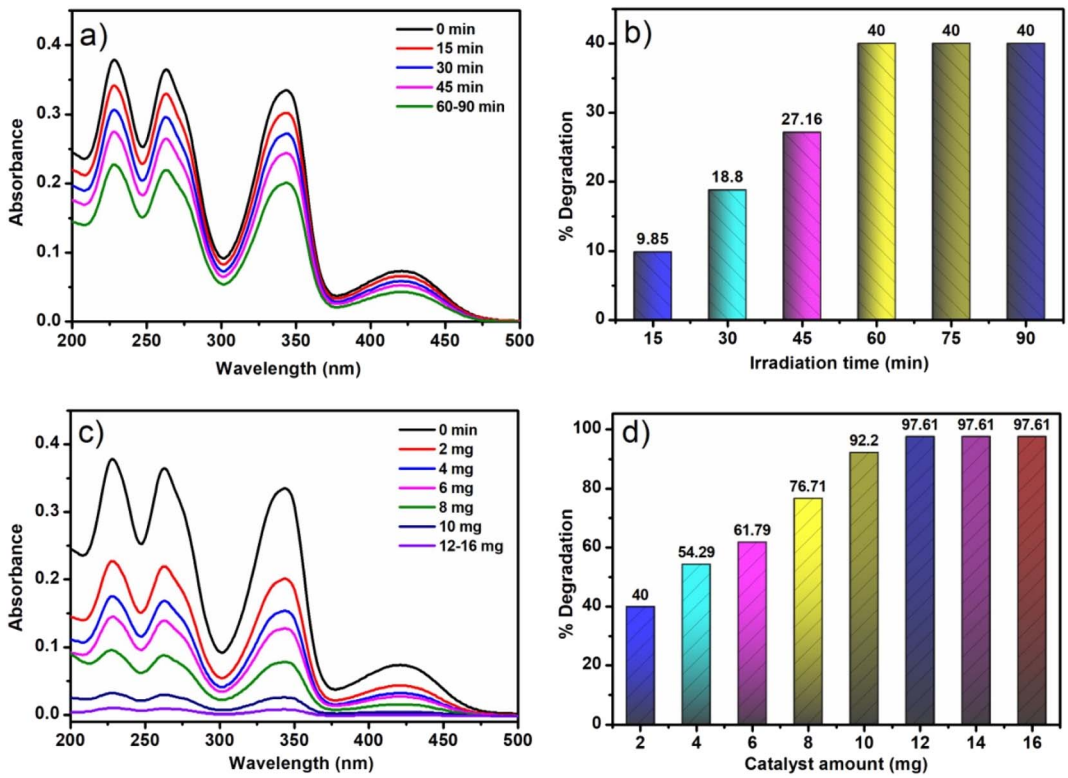

Fig. 7 UV spectra and bar diagram illustrated the effect of (a and b) irradiation time and (c and d) catalyst amount on the photodegradation of 20 mL 50 ppm BH solution at pH = 2 with NFNR/rGO.

© 2025 The Author(s). Published by the Royal Society of Chemistry

Open Access Article. Published on 16 December 2024. Downloaded on 2/8/2026 9:00:53 AM.
This article is licensed under a Creative Commons Attribution-NonCommercial 3.0 Unported Licence.

to be 60 min (Fig. 7a and b). Similarly, upon changing the catalyst amount, 12 mg of the catalyst provided better results at pH = 2 under UV light irradiation for 60 min (Fig. 7c and d).

One significant variable that affects photocatalytic activity is the pH of the reaction system. The pH variations can modify the charge on the surface of the catalysts and the existing form of antibiotics, which can impact the BH breakdown. A comparative BH degradation study with the NFNR/rGO catalyst was performed in order to look into the consequences of pH by varying the pH of the initial reaction medium. Moreover, to study the impact of surface charge of the catalyst, the point of zero charge (pH_{PZC}) was calculated by the batch equilibrium method and was found to be 7.74 (Fig. S7†).[67] It was concluded that when the pH of the initial BH solution was above 7.74, the surface of the catalyst acquired a negative (−ve) charge, whereas the catalyst gains a net positive (+ve) charge on its surface when pH < pH_{PZC}. At low pH, the negatively charged BH ions thereby got strongly attracted to the catalyst surface by the electrostatic force of attraction, increasing the adsorption and degradation efficiency of BH into smaller molecules.[68] Therefore, with all other factors remaining constant, the BH removal effectiveness of the catalyst was 97.61% at pH = 2 and 53.8% at pH = 12 (Fig. S8a and b†). Hence, pH = 2 was determined to be the ideal pH value and applied in the subsequent study.

The methodical assessment of the degradation capacity of NFNR/rGO for BH at varying concentrations is crucial in identifying the highest saturation capacity of the material. This was achieved by examining concentrations ranging from 50 ppm to around 250 ppm keeping other parameters fixed, and the findings are depicted in Fig. S9a.† The degradation potency was observed to decrease when the BH solution concentration was increased (Fig. S9b†). It might be because at larger concentrations, there was more BH adsorption on the catalyst's surface. Moreover, Fig. S9c† illustrates the fitting relation between the concentration of BH and absorbance. The BH degradation process was shown to follow a linear relationship with the increase in BH concentration following the Beer–Lambert law with a correlation coefficient (R^2) value of 0.98.

The BH degradation rate was monitored at a predetermined time span of 10 min to evaluate the reaction kinetics. The degradation process proceeded according to the first-order kinetics (eqn (4)), as shown in Fig. 8a. Furthermore, the logarithm form, as depicted in Fig. 8b, is expressed as follows (k = rate constant):[69]

$$\ln(C_t/C_o) = kt \quad (4)$$

The negative slope of the plot on $\ln(C_t/C_0)$ *vs.* time graph also indicated first-order kinetics for the BH photodegradation reaction with R^2 and k values of 0.98296 and 0.0652 min^{-1}, respectively.

Under optimized conditions, rGO and NFNR showed only 11.34% and 54.11% degradation (Fig. S10a and b†), indicating limited photocatalytic degradation activity. However, the catalytic activity of NFNR/rGO was greater than that of NFNR and rGO when exposed to UV light due to the synergistic impact between them. Further, these catalysts were examined to understand the dynamic behaviours of BH degradation. The appropriate fitting results and the graphs of $\ln(C_o/C_t)$ *vs.* time are displayed in Fig. S10c and d.† The highest rate constant value was found for NFNR/rGO (k = 0.0652 min^{-1}), about 4.8 times and 28 times higher than that of NFNR (0.0134 min^{-1}) and rGO (0.0023 min^{-1}), respectively (Fig. S10e†). For better understanding the photocatalytic activity of the NFNR/rGO composite, a comparison was made with a similar composite material that was prepared by physical mixing of NFNR + rGO. It was characterized again by PXRD and Raman analysis, as provided in ESI (Fig. S11a and b).† Although the characteristic signals in the PXRD and Raman were similar to that of NFNR/rGO synthesized by a hydrothermal method, the activities of these materials were significantly different. As shown in Fig. S11c and d,† the physical mixture of NFNR and rGO showed only 58.7% degradation efficiency. This indicated that the hydrothermally synthesized NFNR/rGO composite was better in the BH photodegradation process. The total decolorization of the BH solution did not prove that the pollutant had fully mineralized into CO_2, H_2O, and NO_3^-. As a result, it was essential to evaluate the catalyst's mineralization efficiency, which was accomplished by determining the total organic content (TOC) before and after photocatalysis.[70] The mineralization efficiency of the catalyst at different time intervals was

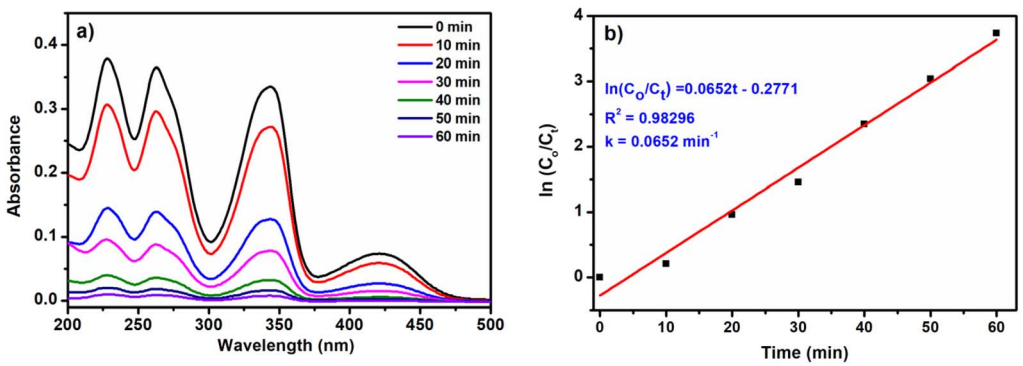

Fig. 8 (a) UV absorption spectra and (b) $\ln(C_o/C_t)$ *vs.* time graph for BH degradation with NFNR/rGO under optimized conditions (12 mg catalyst, 60 min of irradiation time and pH = 2).

Open Access Article. Published on 16 December 2024. Downloaded on 2/8/2026 9:00:53 AM.
This article is licensed under a Creative Commons Attribution-NonCommercial 3.0 Unported Licence.

evaluated by the Walkley and Black titration method, using eqn (2).[71] It was found that, within 30 min of reaction time, only 7.22%, 27.38% and 63.7% of mineralization was observed under darkness, room light and UV light irradiation conditions respectively (Fig. S12†). However, with the increasing UV light irradiation time up to 60 min, almost 83.87% of mineralization had occurred with the NFNR/rGO composite, as shown in Fig. S12.† This finding demonstrated that although the colour of the BH solution was totally bleached under photocatalytic conditions, only 83.87% of BH got mineralized. The remaining 16.13% of BH molecules might have transferred to some other organic species.

In order to understand the possible pathways of degradation of BH under UV light irradiation in the presence of NFNR/rGO catalyst, LCMS and FTIR analysis was performed. The mass spectra recorded before light irradiation showed a sharp signal at an m/z value of 336 corresponding to BH (Fig. 9a). The mass spectra recorded after 20, 40 and 60 min of UV light irradiation in the presence of catalyst are depicted in Fig. 9b–d. It predicted the formation of intermediates A, B, C, E and F. The FTIR spectra were also recorded before and after 60 min of UV light irradiation in the presence of catalyst (Fig. 9e). The FTIR spectra before light irradiation showed a signal at 1035 cm^{-1} due to the C–O–C stretching vibration, 1738 cm^{-1} for the C–O stretching vibration of the five-membered ring, 1365 cm^{-1} and 1442 cm^{-1} for the C–H bending vibrations, and 2983 cm^{-1} and 2915 cm^{-1} assigned to the C–H stretching vibration. However, the FTIR spectra of the bleach solution showed very weak signals, implying the degradation of BH antibiotics. As from the TOC analysis, it was evident that the catalyst can mineralize ~84%. Therefore, the presence of organic contents in the mass spectra as well as in the low-intense FTIR signal appeared due to the remaining non-degraded organic content. Based on this experimental evidence, we propose the degradation pathway as shown in Fig. 9f. Two plausible pathways are shown: in Pathway 1, the intermediate having an m/z value of 295.2 (A, Fig. 9b) was formed by the ring opening of the $-OCH_2O$ group and the loss of the methyl ($-CH_3$) group. Furthermore, the intermediate with an m/z value of 267.2 [B (265) + $2H^+$] (Fig. 9b) was formed as a result of the ring-opening reaction and the loss of a hydroxyl group.[72] Following this, as the photodegradation process preceded, the intermediates with an m/z value of 97.1 [C (94) + $3H^+$] (Fig. 9c) eventually appeared due to the ring-breaking reactions and the disappearance of functional groups. In Pathway 2, a species with an m/z value of 307 was probably produced, because of the elimination of the methoxy methyl radical. After that, the product with an m/z value of 307 got converted to the other intermediate by eliminating the methyl radicals and CO. Over the course of the reaction, an open-ring reaction and release of functional groups yielded the intermediates: $m/z = 139.1$ [E (135) + $4H^+$] and $m/z = 130.2$ [F (129) + H^+] (Fig. 9d).[27]

5. Recyclability test

The photostability and reusability are two essential parameters of a photocatalyst. The synthesized NFNR/rGO photocatalyst was magnetically separable, as shown in Fig. 10a. Using the magnetic separation approach, the catalyst and reaction mixture were readily separable. The cycle degradation studies of BH were conducted for five times with the NFNR/rGO heterojunction (Fig. 10b). After each photocatalytic reaction,

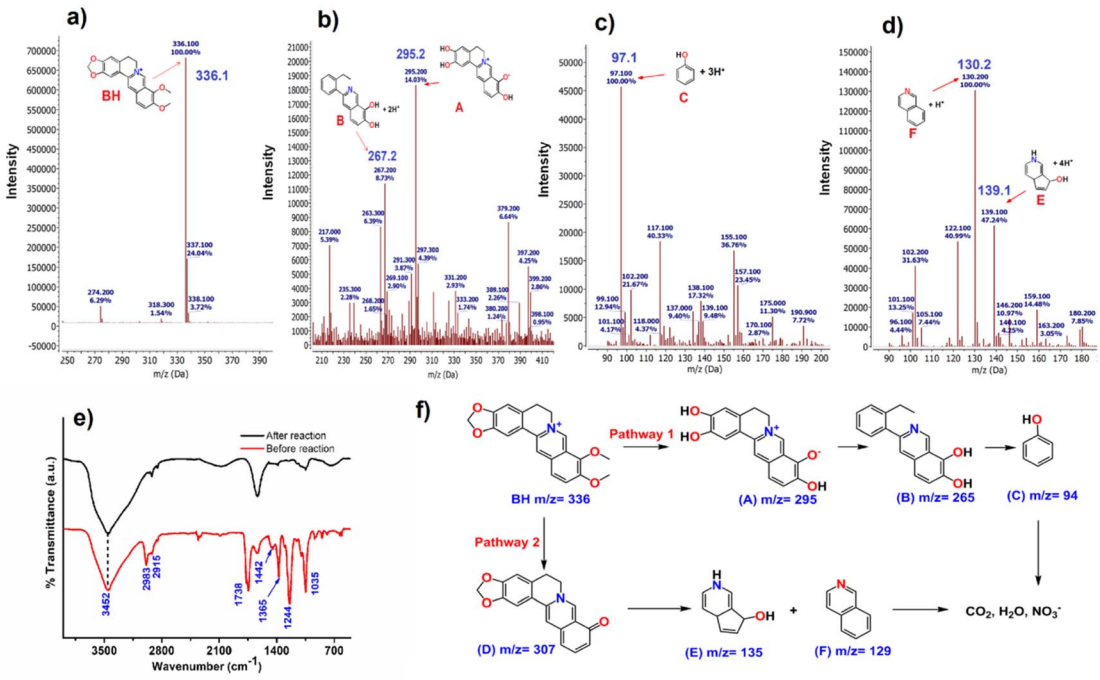

Fig. 9 Mass spectra showing an m/z value of (a) BH, (b) intermediates A and B, (c) C and (d) E and F, (e) FTIR spectra of the reaction mixture before and after UV light irradiation, and (f) proposed degradation pathways of BH over NFNR/rGO.

© 2025 The Author(s). Published by the Royal Society of Chemistry

Open Access Article. Published on 16 December 2024. Downloaded on 2/8/2026 9:00:53 AM.
This article is licensed under a Creative Commons Attribution-NonCommercial 3.0 Unported Licence.

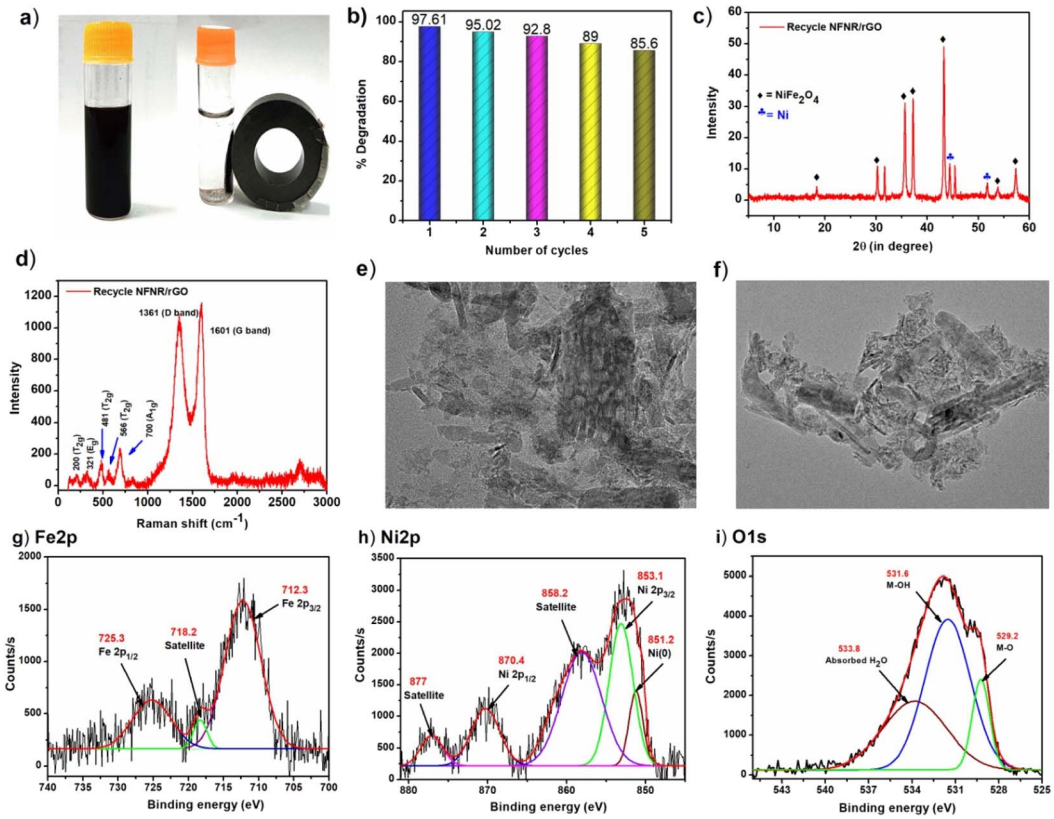

Fig. 10 (a) Magnetic separation and recycling technique, (b) % degradation of BH up to 5th cycle, (c) PXRD analysis, (d) Raman spectra, (e and f) TEM images, and XPS spectra of (g) Fe 2p, (h) Ni 2p and (i) O 1s of recycled NFNR/rGO.

powdered catalysts were recovered and utilized again for the subsequent photocatalytic reactions under the same conditions to examine the photostability and recyclability of the composite. It was found that the NFNR/rGO composite exhibited high stability and photocatalytic activity throughout the reaction cycles (Fig. 10b). The ability of the NFNR/rGO catalyst to degrade the BH molecules retained well up to the second cycle with 95.02% efficiency. However, the catalyst's ability to degrade BH decreased in each subsequent cycle, reaching a maximum of 85.6% in the 5th cycle. The cause for the drop in degradation efficiency was attributed to a certain quantity of catalyst being lost during the magnetic separation procedure. Further the leaching of Fe and Ni was tested by potassium ferricyanide and dimethyl glyoxime (DMG) tests, respectively. Both the tests were found to be negative as shown in Fig. S13,† indicating that the NFNR/rGO catalyst was quite stable under strong acidic conditions (pH = 2).

The recyclable catalyst was further characterized by PXRD, Raman, TEM and XPS analyses. The PXRD spectra showed all the characteristic peaks of NFNR/rGO along with two additional peaks at $2\theta = 44.3°$ and 51.7° assigned to metallic Ni (JCPDS no.: 00-001-1258) (Fig. 10c). The Stokes lines in the Raman spectra resembled with the fresh catalyst (Fig. 10d). However, $I_D/I_G = 0.91$ in the recycled NFNR/rGO composite was found to decrease in comparison to the fresh catalyst, for which $I_D/I_G = 0.98$ (Fig. 1b), indicating the decrease in the degree of disorder in rGO.[73] TEM analysis of the recycled NFNR/rGO composite displayed some structural deformation, as shown in Fig. 10e and f. The leaching of nickel content as metallic nickel and re-adsorption on the catalyst, the deformation of the carbon matrix as well as the loss of small content of the catalyst during magnetic separation might probably cause a decrease in the photodegradation ability of the recycled catalyst. However, it is to be noted that the retention of the PXRD and Raman signals along with the structural morphology suggested that the catalyst was quite stable to prolonged exposure to UV light (~300 min for 5 cycles, each cycle of 60 min). In the XPS spectra of the recycled catalyst, the BE values were found to be approximately similar to that of the fresh catalyst (Fig. 10g–i). The presence of Ni(0) in the Ni 2p spectra was in accordance with the PXRD analysis further confirming the leaching of nickel as metallic nickel (Fig. 10h).

6. Mechanistic study

To determine the impact of reactive groups and comprehend the photodegradation mechanism for BH degradation by the NFNR/rGO catalyst, several scavenging agents for e^-, h^+ and free radicals were added to the reaction medium. Herein, 1 mM of silver nitrate ($AgNO_3$) was utilized for quenching e^-, potassium iodide (KI) was for h^+ scavenger, while ascorbic acid and isopropanol were utilized as radical scavengers for the $O_2^{-\bullet}$ and

Open Access Article. Published on 16 December 2024. Downloaded on 2/8/2026 9:00:53 AM. This article is licensed under a Creative Commons Attribution-NonCommercial 3.0 Unported Licence.

OH˙ radicals, respectively.[74] The outcomes demonstrated that there was a minimal effect on the photodegradation of BH with the addition of KI and $AgNO_3$. However, adding ascorbic acid and isopropanol to the reaction medium dramatically reduced the photocatalytic activity of NFNR/rGO (Fig. S14†). Therefore, during the photocatalytic degradation of BH by NFNR/rGO nanocomposites under the influence of UV light, the two primary active species that should be involved were $O_2^{-\cdot}$ and OH˙ radicals. The Electron Spin Resonance (EPR) spectrum recorded before and after addition of the free radical trapping agent 5,5-dimethyl-1-pyrroline N-oxide (DMPO) is shown in Fig. S15a and b.† The EPR spectrum displayed in Fig. S15a† shows a sharp signal with $g_\perp$ and $g_\parallel$ values of 2.0048 and 2.0089, respectively in the magnetic field region of 320–350 mT for a free radical species, which may be for $O_2^{-\cdot}$ or OH˙ radicals. After the addition of DMPO, a sextet hyperfine structure was observed as characteristic of DMPO–$O_2^{-\cdot}$ adduct (Fig. S15b†).[75] The EPR analysis thus confirmed the generation of active free radicals in the photodegradation process.

The terephthalic acid (TA) test further established the production of OH˙ radicals.[76] A TA solution was prepared by adding 1 mmol of TA in 0.1 M NaOH solution. Subsequently, 20 mL of reaction mixture (BH + catalyst) was mixed with the TA solution by magnetic stirring and subjected to irradiation. When TA interacted with OH˙ radicals, fluorescent hydroxyl terephthalic acid (HTA) was generated. As depicted in Fig. 11a, the production of HTA during the photodegradation process was verified by the development of a PL emission peak at about 433 nm at an excitation wavelength of 315 nm.

Based on the results obtained from the Mott–Schottky analysis and various scavenging agent tests, a plausible mechanism for the photocatalytic degradation of BH using the NFNR/rGO composite is illustrated in Fig. 11c. At first, owing to the presence of different functional groups in rGO, the BH molecules got adsorbed onto the rGO nanosheets. Besides, the BH molecules interacted with the 2D matrix through π–π interactions (Fig. 11b). Upon irradiation of UV light on the material surface, electrons from the VB of the NFNR got excited to the CB, leaving the positively charged holes in the VB of the NFNR. The Fe_2O_3 impurity present in the material might have helped in facilitating the separation of photogenerated electrons in the CB from the holes in the VB by shuttling their oxidation state between Fe^{III} and Fe^{II}. Additionally, electrons from the CB of the NFNR may get transferred to the rGO surface aided by the Fe^{III}/Fe^{II} couple, as shown in Fig. 11c, thereby increasing the electron density in the CB of rGO. From the theoretical calculation, it was found that the Fermi levels in the rGO, NFNR and NFNR/rGO lie at −3.5 eV, −3.7 eV and −3.0 eV, respectively. Since the Fermi level of the NFNR and rGO was found to be comparable, which might also have facilitated the generation of internal electric field (IEF) and favoured the electron transfer from the NFNR to rGO. The electrons at the rGO surface reacted with O_2 to produce the active superoxide radical anion ($O_2^{\cdot -}$). This was possible as the V_{CB} of rGO (−0.65 V) was found to be more negative than $O_2/O_2^{-\cdot}$ ($E_{O_2/O_2^{-\cdot}}$ = −0.18 V *vs.* RHE).[77] In an

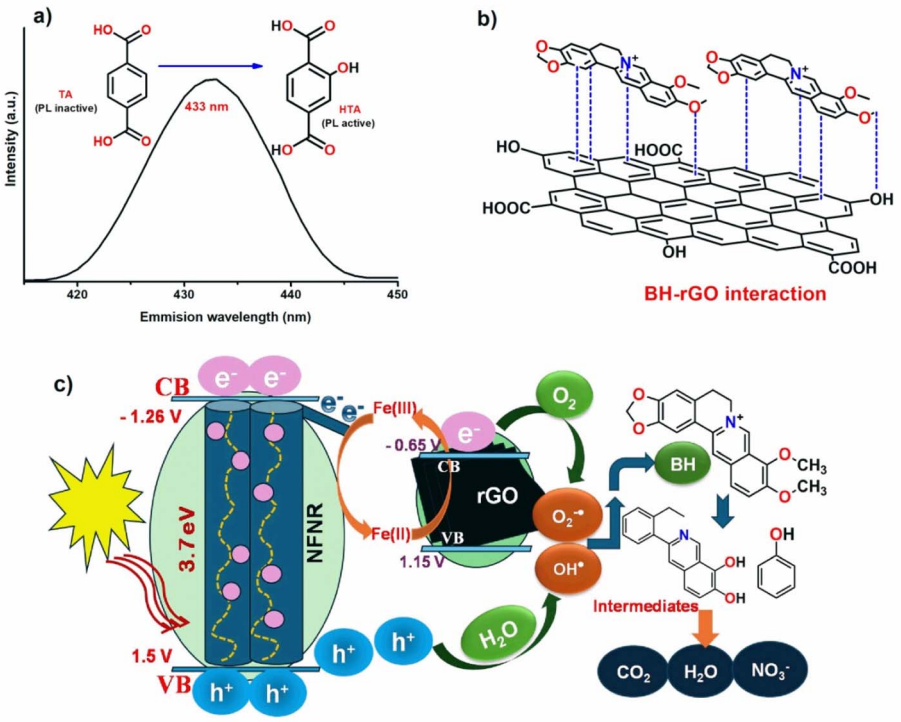

Fig. 11 (a) PL spectra indicated the formation of hydroxyl terephthalic acid (HTA), (b) BH-rGO π–π interactions and (c) plausible mechanism for the photocatalytic degradation of BH on the NFNR/rGO surface under UV light irradiation.

© 2025 The Author(s). Published by the Royal Society of Chemistry

Open Access Article. Published on 16 December 2024. Downloaded on 2/8/2026 9:00:53 AM. This article is licensed under a Creative Commons Attribution-NonCommercial 3.0 Unported Licence.

Table 2 First-order rate constants for the photocatalytic BH degradation

Materials	% Degradation	Correlation coefficient value (R^2)	k for BH degradation (min^{-1})
NiO/rGO	8.45	0.99	0.0015
Fe_2O_3/rGO	16.9	0.92	0.0031
NFNR-1/rGO	53.52	0.92	0.0111
NFNR-2/rGO	61.97	0.98	0.0153
NFNR/CTW	78.87	0.91	0.0235
NFNR/rGO	**97.61**	**0.95**	**0.0652**

aqueous environment, these superactive $O_2^{\bullet-}$ radicals took part in the degradation of BH molecules into smaller molecules such as CO_2, H_2O, and NO_3^- through some intermediates, as predicted in Fig. 9b–f.

7. Comparative study

The photodegradation reaction of BH was also studied by using other synthesized catalysts, namely NFNR-1/rGO, NFNR-2/rGO and NFNR/CTW. All the synthesized materials were analyzed by PXRD, Raman, FTIR spectroscopy, TGA and SEM EDX analysis, and the results are provided in the ESI.† The PXRD pattern of NFNR-1/rGO showed the presence of both Fe_2O_3 and $NiFe_2O_4$. Similarly, NFNR-2/rGO contained NiO components along with $NiFe_2O_4$, as confirmed from the JCPDS data of NiO (Fig. S16a and b†). The Raman spectra of the materials showed the presence of D and G bands for carbon materials and all other peaks are shown in Fig. S17 and Table S1.† The FTIR spectra are provided in Fig. S18,† and the peak assignments are summarized in Table S2.† The TGA spectra depicted the thermal stability of the materials (Fig. S19†). The presence of all the elements in NFNR-1/rGO, NFNR-2/rGO and NFNR/CTW was confirmed by SEM-EDX analysis, as shown in Fig. S20.†

The photodegradation reaction for the BH molecule was carried out with all these synthesized materials, and the findings are given in Fig. S21a–e.† It was found that the NFNR/rGO composite showed the maximum degradation rate under the optimized conditions. The rate of the reaction drops to 0.0235 min^{-1} when the rGO support was substituted by CTW (carbon material derived from tea leaf wastes). Similarly, the rate of the reaction with other materials decreased in the order of NFNR/rGO > NFNR/CTW > NFNR-1/rGO > NFNR-2/rGO > Fe_2O_3 > NiO. It further revealed that a higher Ni content and NiO as impurity lower the activity of the catalyst. Table 2 provides the % degradation of BH, k and R^2 values for each material. The kinetic variables for all the six synthesized catalysts for BH degradation are displayed in Fig. S21c and d.†

The activity of our synthesized catalyst was also compared with the other reported results, as given in Table S3.† For example, the $NiFe_2O_4$ composite with Ag and gC_3N_4 degraded tetracycline within 120 min of visible light irradiation (Table S3,† entry no 4). Similarly, $NiFe_2O_4$-degraded Pharmaceutical SSX up to 74% within 120 min under visible light (Table S3,† entry no 6). The high photodegradation ability and good mineralization efficiency of the present material can be attributed to the one-dimensional nanorod combined with two-dimensional rGO. Since the charge carrying ability of 1D–2D nanohybrids is better, in the present material, the combination of such nanomatrixes might have significantly improved the photodegradation process.[2] In comparison to the literature reports provided in Table S3,† it can be said that by tuning the morphology of $NiFe_2O_4$, the charge carrier matrix can yield an affordable photocatalyst for the degradation of BH in a short irradiation time.

8. Conclusion

In summary, it can be said that an NFNR with a 1D nanorod structure with an average diameter of 10–20 nm and an average length of 70–90 nm was found to be a good photocatalyst for the degradation of BH. The activity of the material was found to profoundly improve upon combination with 2D rGO nanosheets derived from waste battery materials. The rate constant value for BH degradation over NFNR/rGO was 0.0652 min^{-1}, which was 4.8 times and 28 times higher than that of NFNR and rGO, respectively. The mass spectrometric investigation allowed us to conclude that the hybrid composite can degrade BH to CO_2, H_2O, and NO_3^- through the formation of various intermediate compounds. The BH mineralization of 83.87% suggested the high efficacy of the material in the degradation process. The mechanistic pathway of the photocatalytic degradation process revealed that the primary active species were $O_2^{\bullet-}$ radicals and $OH^{\bullet}$ radicals. More significantly, the band edge potential supported the entire photochemical process and was sufficient to facilitate H_2O oxidation. The degradation activity of the material decreased when rGO was replaced with CTW and also with the variation of Ni and Fe ratio. Leaching of nickel, decrease in disorder in rGO and deformation of nanorods influenced the photodegradation capacity in the recycled catalyst. Further, from the comparison with other synthesized catalysts, it was evident that a high nickel content or Ni as impurity lowers the activity of the catalyst.

Data availability

Data will be provided upon request.

Open Access Article. Published on 16 December 2024. Downloaded on 2/8/2026 9:00:53 AM. This article is licensed under a Creative Commons Attribution-NonCommercial 3.0 Unported Licence.

Author contributions

Sayanika Saikia: methodology, validation, formal analysis, investigation, writing – original draft, writing – review & editing; Salma A. Khanam: formal analysis, investigation; Priyanuj Kandali: formal analysis; Ankur Kanti Guha: data curation, software, Kusum K. Bania: conceptualization, writing – original draft, writing – review & editing visualization, supervision, project administration, funding acquisition.

Conflicts of interest

There are no conflicts to declare.

Acknowledgements

KKB acknowledges Anusandhan National Research Foundation (ANRF) for research grants CRG/2023/000957, EEQ/2023/000350 and CSIR (No. 80(0094)/20/EMR-II). S. Saikia expresses her gratitude to the University Grants Commission (UGC) for Junior Research Fellowship. Authors would also like to appreciate the Tezpur University for giving the analytical and infrastructural facilities required for this research work.

References

1 F. Seifikar and A. Habibi-Yangjeh, *Chemosphere*, 2024, **355**, 141686.
2 Y. Zhong, C. Peng, Z. He, D. Chen, H. Jia, J. Zhang, H. Ding and X. Wu, *Catal. Sci. Technol.*, 2021, **11**, 27–42.
3 B. Weng, S. Liu, Z. R. Tang and Y. J. Xu, *Rsc Adv.*, 2014, **4**, 12685–12700.
4 R. Lakshmi Priya and S. Ganesh Babu, *Langmuir*, 2024, **40**, 10293–10304.
5 J. Di, J. Xia, M. F. Chisholm, J. Zhong, C. Chen, X. Cao, F. Dong, Z. Chi, H. Chen, Y. X. Weng and J. Xiong, *Adv. Mater.*, 2019, **31**, 1807576.
6 M. Tahir, B. Tahir, M. G. M. Nawawi, M. Hussain and A. Muhammad, *Appl. Surf. Sci.*, 2019, **485**, 450–461.
7 K. Yu, X. Pan, G. Zhang, X. Liao, X. Zhou, M. Yan, L. Xu and L. Mai, *Adv. Energy Mater.*, 2018, **8**, 1802369.
8 B. Liu, A. Khare and E. S. Aydil, *ACS Appl. Mater. Interfaces*, 2011, **3**, 4444–4450.
9 N. Goodarzi, Z. Ashrafi-Peyman, E. Khani and A. Z. Moshfegh, *Catalysts*, 2023, **13**, 1102.
10 A. Hezam, K. Alkanad, M. A. Bajiri, J. Strunk, K. Takahashi, Q. A. Drmosh, N. Al-Zaqri and L. N. Krishnappagowda, *Small Methods*, 2023, **7**, 2201103.
11 I. Ahmad, S. Shukrullah, M. Y. Naz, F. K. Alsaif, S. Alsulamy, Y. Khan, N. R. Khalid and W. Q. Khan, *Mater. Sci. Semicond. Process.*, 2023, **159**, 107392.
12 J. Li, Z. Li, Y. Song, X. Zhang, H. Xie, S. Sheng and H. Zou, *Inorg. Chem.*, 2024, **63**(23), 10568–10584.
13 Z. H. Jabbar, A. A. Okab, B. H. Graimed, S. H. Ammar, H. Taofeeq and A. A. Mohammed, *Sol. Energy*, 2024, **277**, 112751.
14 A. Pramanik, J. A. Dhar, R. Banerjee, M. Davis, K. Gates, J. Nie, D. Davis, F. X. Han and P. C. Ray, *ACS Appl. Bio Mater.*, 2023, **6**, 919–931.
15 N. Wetchakun, S. Chaiwichain, B. Inceesungvorn, K. Pingmuang, S. Phanichphant, A. I. Minett and J. Chen, *ACS Appl. Mater. Interfaces*, 2012, **4**, 3718–3723.
16 J. Di, C. Zhu, M. Ji, M. Duan, R. Long, C. Yan, K. Gu, J. Xiong, Y. She, J. Xia and H. Li, *Angew. Chem., Int. Ed.*, 2018, **57**, 14847–14851.
17 M. G. Idris, H. Y. Hafeez, J. Mohammed, A. B. Suleiman and C. E. Ndikilar, *Appl. Surf. Sci. Adv.*, 2023, **18**, 100468.
18 C. Dharmaraja, P. E. Nicholas, P. Ramya, I. I. Premkumar, V. Vijayan and N. Senthilkumar, *Inorg. Chem. Commun.*, 2021, **126**, 108481.
19 H. L. Andersen, C. Granados-Miralles, K. M. Jensen, M. Saura-Múzquiz and M. Christensen, *ACS Nano*, 2024, **18**, 9852–9870.
20 Z. He, Y. Xia, B. Tang, J. Su and X. Jiang, *Z. Phys. Chem.*, 2019, **233**(3), 347–359.
21 J. Luo, X. Zhou, F. Yang, X. Ning, L. Zhan, Z. Wu and X. Zhou, *J. Clean. Prod.*, 2022, **357**, 131992.
22 Z. He, Y. Xia, J. Su and B. Tang, *Opt. Mater.*, 2019, **88**, 195–203.
23 Y. Xia, Z. He, Y. Lu, B. Tang, S. Sun, J. Su and X. Li, *RSC Adv.*, 2018, **8**, 5441–5450.
24 M. B. Taj, M. D. Alkahtani, A. Raheel, S. Shabbir, R. Fatima, S. Aroob, R. Yahya, W. Alelwani, N. Alahmadi, M. Abualnaja and S. Noor, *Sci. Rep.*, 2021, **11**, 5439.
25 S. Patar, R. Mittal, F. Yasmin, B. K. Bhuyan and L. J. Borthakur, *Chemosphere*, 2024, **363**, 142908.
26 C. Kalita, P. K. Boruah, M. R. Das and P. Saikia, *Inorg. Chem. Commun.*, 2022, **146**, 110073.
27 Y. Yu, W. Xu, J. Fang, D. Chen, T. Pan, W. Feng, Y. Liang and Z. Fang, *Appl. Catal., B*, 2020, **268**, 118751.
28 I. E. Allijn, R. Oldenkamp, G. Storm, A. M. Ragas and R. M. Schiffelers, *PLoS One*, 2018, **13**, e0199095.
29 W. Qin, Y. Song, Y. Dai, G. Qiu, M. Ren and P. Zeng, *Environ. Earth Sci.*, 2015, **73**, 4939–4946.
30 P. Li, L. Qin, T. Wang, L. Dai, H. Li, J. Jiang, J. Zhou, H. Li, X. Cheng and F. Lei, *Chem. Eng. J.*, 2020, **392**, 123707.
31 C. B. Xu, T. Dong, X. P. Ma, F. Ma, Q. Zhao, L. Wang and K. Bao, *Environ., Energy Sustainable Dev.*, 2013, **4**, 235.
32 M. Ren, Y. Song, S. Xiao, P. Zeng and J. Peng, *Chem. Eng. J.*, 2011, **169**, 84–90.
33 E. S. da Silva, M. C. V. M. Starling and C. C. Amorim, *Environ. Sci. Pollut. Res.*, 2023, 1–23.
34 Y. Ahmed, J. Zhong, Z. Wang, L. Wang, Z. Yuan and J. Guo, *Environ. Sci. Technol.*, 2022, **56**, 15156–15166.
35 C. Zhang, X. Ren, K. Wang, X. Liang, Y. Wu and Y. He, *Ceram. Int.*, 2024, **50**, 43340–43344.
36 C. Zhao, C. Wang, X. Ren, S. Yuan, L. Zhao, L. Zhuang, B. Teng, Y. Wu and Y. He, *Chem. Eng. J.*, 2024, **498**, 155202.
37 X. Ren, Y. Chu, S. Yuan, Y. Zheng, Z. Zeng, C. Xia, L. Zhao, Y. Wu and Y. He, *J. Environ. Manage.*, 2024, **370**, 122776.
38 Y. Chu, C. Zhao, Y. Zheng, X. Ren, S. Yuan, L. Zhao, Y. Wu and Y. He, *J. Environ. Sci.*, 2024, DOI: **10.1016/j.jes.2024.08.033**.

© 2025 The Author(s). Published by the Royal Society of Chemistry

Open Access Article. Published on 16 December 2024. Downloaded on 2/8/2026 9:00:53 AM. This article is licensed under a Creative Commons Attribution-NonCommercial 3.0 Unported Licence.

39 J. Luo, K. Wang, Y. Qiu, X. Zhou, X. Ning, L. Zhan and X. Zhou, *J. Alloys Compd.*, 2024, **1008**, 176572.
40 J. Luo, J. Chen, X. Chen, X. Ning, L. Zhan and X. Zhou, *J. Colloid Interface Sci.*, 2021, **587**, 831–844.
41 K. Rabé, L. Liu, N. A. Nahyoon, Y. Zhang and A. M. Idris, *Sep. Purif. Technol.*, 2019, **212**, 774–782.
42 G. Gogoi, S. Saikia, A. Das, S. Saikia, N. Hoque, S. Biswas, M. Dey, P. K. Kalita and K. K. Bania, *ChemistrySelect*, 2023, **8**, e202300279.
43 M. J. Baruah, T. J. Bora, G. Gogoi, N. Hoque, N. K. Gour, S. K. Bhargava, A. K. Guha, J. K. Nath, B. Das and K. K. Bania, *J. Colloid Interface Sci.*, 2022, **608**, 1526–1542.
44 S. A. Khanam, K. Sarmah, A. K. Guha, S. Lee, Y. B. Park, L. Saikia, S. Saikia, R. A. Saha and K. K. Bania, *Electrochim. Acta*, 2024, **498**, 144641.
45 S. Biswas, D. Barman, G. Gogoi, N. Hoque, A. Devi, S. K. Purkayastha, A. K. Guha, J. K. Nath and K. K. Bania, *Org. Biomol. Chem.*, 2023, **21**, 1657–1661.
46 A. Zeyede, *J. Soil Sci. Environ.*, 2020, **11**, 1–5.
47 Y. Zhao and D. G. Truhlar, *Theor. Chem. Acc.*, 2008, **120**, 215–241.
48 M. J. Frisch, G. W. Trucks, H. B. Schlegel, G. E. Scuseria, M. A. Robb, J. R. Cheeseman, G. Scalmani, V. Barone, G. A. Petersson, H. Nakatsuji, X. Li, M. Caricato, A. V. Marenich, J. Bloino, B. G. Janesko, R. Gomperts, B. Mennucci, H. P. Hratchian, J. V. Ortiz, A. F. Izmaylov, J. L. Sonnenberg, D. Williams-Young, F. Ding, F. Lipparini, F. Egidi, J. Goings, B. Peng, A. Petrone, T. Henderson, D. Ranasinghe, V. G. Zakrzewski, J. Gao, N. Rega, G. Zheng, W. Liang, M. Hada, M. Ehara, K. Toyota, R. Fukuda, J. Hasegawa, M. Ishida, T. Nakajima, Y. Honda, O. Kitao, H. Nakai, T. Vreven, K. Throssell, J. A. Montgomery Jr, J. E. Peralta, F. Ogliaro, M. J. Bearpark, J. J. Heyd, E. N. Brothers, K. N. Kudin, V. N. Staroverov, T. A. Keith, R. Kobayashi, J. Normand, K. Raghavachari, A. P. Rendell, J. C. Burant, S. S. Iyengar, J. Tomasi, M. Cossi, J. M. Millam, M. Klene, C. Adamo, R. Cammi, J. W. Ochterski, R. L. Martin, K. Morokuma, O. Farkas, J. B. Foresman and D. J. Fox, *Gaussian 16*, revision A.03, Gaussian, Inc., Wallingford, CT, 2016.
49 T. Lu and F. Chen, *J. Comput. Chem.*, 2012, **33**, 580.
50 L. Stobinski, B. Lesiak, A. Malolepszy, M. Mazurkiewicz, B. Mierzwa, J. Zemek, P. Jiricek and I. Bieloshapka, *J. Electron Spectrosc. Relat. Phenom.*, 2014, **195**, 145–154.
51 S. Mishra, P. Kumar and S. K. Samanta, *Ind. Eng. Chem. Res.*, 2020, **59**, 15839–15847.
52 J. L. Ortiz-Quiñonez, U. Pal and M. S. Villanueva, *ACS Omega*, 2018, **3**, 14986–15001.
53 E. Rommozzi, M. Zannotti, R. Giovannetti, C. A. D'Amato, S. Ferraro, M. Minicucci, R. Gunnella and A. Di Cicco, *Catalysts*, 2018, **8**(12), 598.
54 P. Xiong, Y. Fu, L. Wang and X. Wang, *Chem. Eng. J.*, 2012, **195**, 149–157.
55 A. B. Garg, D. Vie, P. Rodriguez-Hernandez, A. Muñoz, A. Segura and D. Errandonea, *J. Phys. Chem. Lett.*, 2023, **14**, 1762–1768.
56 P. S. Abid, S. S. Islam, P. Mishra and S. Ahmad, *Sci. Rep.*, 2018, **8**(1), 3537.
57 Z. Iqbal, M. S. Tanweer and M. Alam, *ACS Omega*, 2023, **8**, 6376–6390.
58 L. T. M. Thy, N. T. C. Linh, N. T. T. Tram, T. H. Tu, L. T. Tai, P. T. Khang, H. M. Nam, N. H. Hieu and M. T. Phong, *J. Nanomater.*, 2021, **2021**, 4636531.
59 M. Khairy and M. E. Gouda, *J. Adv. Res.*, 2015, **6**, 555–562.
60 D. Xu, S. N. Zhang, J. S. Chen and X. H. Li, *Chem. Rev.*, 2022, **123**, 1–30.
61 T. Wang, J. Liu, P. Wu, C. Feng, D. Wang, H. Hu and G. Xue, *J. Mater. Chem. A*, 2020, **8**, 16590–16598.
62 Y. Li, Z. Zhang, L. Pei, X. Li, T. Fan, J. Ji, J. Shen and M. Ye, *Appl. Catal., B*, 2016, **190**, 1–11.
63 Z. Zhong, D. You, Y. Wan, Z. Pan and Q. Cheng, *Inorg. Chem.*, 2024, **63**, 14509–14524.
64 Z. Iqbal, M. S. Tanweer and M. Alam, *ACS Omega*, 2023, **8**, 6376–6390.
65 R. Sankaranarayanan, S. Shailajha, M. K. Mubina and C. P. Anilkumar, *J. Supercond. Novel Magn.*, 2020, **33**, 3631–3642.
66 S. V. Bhosale, P. S. Ekambe, S. V. Bhoraskar and V. L. Mathe, *Appl. Surf. Sci.*, 2018, **441**, 724–733.
67 S. Saikia, M. Saikia, S. A. Khanam, S. Lee, Y. B. Park, L. Saikia, G. Gogoi and K. K. Bania, *Mater. Adv.*, 2023, **4**, 6244–6258.
68 S. Saikia, L. Saikia, S. Lee, Y. B. Park, R. A. Saha, S. A. Khanam, M. E. Zaki and K. K. Bania, *J. Environ. Chem. Eng.*, 2024, **12**, 112344.
69 V. Ramar and K. Balasubramanian, *ACS Appl. Nano Mater.*, 2021, **4**, 5512–5521.
70 W. Kang, S. Chen, H. Yu, T. Xu, S. Wu, X. Wang, N. Lu, X. Quan and H. Liang, *J. Hazard. Mater.*, 2021, **405**, 124277.
71 G. Gogoi, P. Saikia, M. J. Baruah, S. Lee, Y. B. Park, R. Dutta and K. K. Bania, *Microporous Mesoporous Mater.*, 2021, **326**, 111392.
72 Y. Zhang, L. Liu, B. Van der Bruggen, M. K. Leung and F. Yang, *Chem. Eng. J.*, 2019, **373**, 179–191.
73 A. Maulana, A. Y. Nugraheni, D. N. Jayanti, S. Mustofa and M. A. Baqiya, *IOP Conf. Ser. Mater. Sci. Eng.*, 2017, **196**, 012021.
74 Z. Huang, S. Jia, J. Wei and Z. Shao, *RSC Adv.*, 2021, **11**, 16747–16754.
75 Z. He, H. Yang, J. Su, Y. Xia, X. Fu, L. Wang and L. Kang, *Fuel*, 2021, **294**, 120399.
76 G. Žerjav, A. Albreht, I. Vovk and A. Pintar, *Appl. Catal. Gen.*, 2020, **598**, 117566.
77 S. Cheeseman, A. J. Christofferson, R. Kariuki, D. Cozzolino, T. Daeneke, R. J. Crawford, V. K. Truong, J. Chapman and A. Elbourne, *Adv. Sci.*, 2020, **7**, 1902913.

© 2025 The Author(s). Published by the Royal Society of Chemistry